

**On the Regulation of the Geospace System by
Solar-Wind/IMF Discontinuities and
Ionospheric Outflow**

by

Yiqun Yu

A dissertation submitted in partial fulfillment
of the requirements for the degree of
Doctor of Philosophy
(Space and Planetary Physics)
in the University of Michigan
2011

Doctoral Committee:

Associate Professor Aaron J. Ridley, Chair
Professor Mark Moldwin
Associate Professor Mike W. Liemohn
Assistant Professor James W. Cutler
Research Professor Margaret G. Kivelson
Research Associate Professor Kenneth C. Hansen

© Yiqun Yu 2011
All Rights Reserved

To my mother, for blessing me these years.

ACKNOWLEDGEMENTS

During the past few years of my Ph.D study, I have been constantly receiving help from many people, without whom this dissertation would not have been completed. Upon the approach of my Ph.D degree, I would really like to thank them for their support.

I owe my deepest gratitude to my academic advisor Professor Aaron J. Ridley who has made available his support in a number of ways. He led me into the scientific wonderland with his endless enthusiasm and frankness and instructed me with his broad knowledge, proficient techniques and profound insight. I really appreciate his sensible training on me from the beginning, his countless valuable advises any time I am in need, his encouragements to help me build up confidence during depression times, and his kindness on me all the time. I have greatly enjoyed the comfortable and efficient working atmosphere with Professor Ridley who possesses a sense of humor and a cheerful character that can light up the surrounding. I often felicitate myself on my decision years ago to come to Michigan and have Professor Ridley as my doctoral advisor.

It is an honor for me to have Professors Mark Moldwin, Michael Liemohn, James Cutler, Margaret Kivelson, and Kenneth Hansen in my doctoral committee to evaluate my research work. Also I would like to thank Darren De Zeeuw and Gabor Toth for their professional and inspiring help in the computational techniques.

I am indebted to many graduate student fellows in our department with whom I have had a great time in AOSS and Ann Arbor, including David Pawlowski, Amanda

Brecht, Yuxing Yun, Xi Chen, Tami McDunn, Liang Zhao, Cheng Zhou, Raluca Ilia, Dalal Najib, Dan Welling, Alex Glocer, Ofer Cohen, to name a few. Special thanks are given to our secretaries who helped me through a lot of tedious processes in these years: Jan Beltran, Margaret Reid, Genel Frye, and Susan Griffin.

Lastly, I want to express plenty of gratitude to my father Jinhai Yu, who has been spiritually supporting me ever since I stepped onto the airplane at Shanghai and constantly showing confidence in me all these years.

TABLE OF CONTENTS

DEDICATION	ii
ACKNOWLEDGEMENTS	iii
LIST OF FIGURES	viii
ABSTRACT	xiii
CHAPTER	
I. Introduction	1
1.1 Solar wind-magnetosphere coupling	1
1.2 Magnetosphere-ionosphere coupling	8
1.2.1 High-latitude electromagnetic coupling	10
1.2.2 High-latitude mass coupling	15
1.3 Magnetic storms and substorms	17
1.4 Motivation	19
1.4.1 Space weather prediction	20
1.4.2 Importance of the solar wind density	21
1.4.3 The impact of ionospheric outflow	21
1.5 Dissertation structure	24
II. Methodology:	
Space Weather Modeling Framework	25
2.1 SWMF introduction	25
2.2 Near-Earth modules	26
2.2.1 Global magnetosphere (GM)	28
2.2.2 Ionospheric electrodynamics (IE)	33
2.2.3 Inner magnetosphere (IM)	35
2.3 My contribution to the SWMF	38
III. Response to IMF Bz change: Reaction Delay	40

3.1	Introduction	41
3.2	Simulation results	43
3.2.1	Ionosphere	43
3.2.2	IMF transition propagation and reconnection	47
3.2.3	Ground magnetic perturbations	53
3.3	Discussion and summary	54
IV. Response to a Sudden Increase in the Solar Wind Density: Generation Mechanisms		60
4.1	Introduction	60
4.2	Methodology	65
4.3	Simulation results	66
4.3.1	Results with northward IMF conditions	66
4.3.2	Results with southward IMF conditions	67
4.4	Discussion	74
4.4.1	First phase	74
4.4.2	Second phase	79
4.5	Conclusions	88
V. Understanding the Response to a Sudden Increase in the So- lar Wind Density		90
5.1	Introduction	90
5.2	Observations	94
5.2.1	Two observational examples	95
5.2.2	Statistical view	99
5.3	Simulations with different Alfvén Mach numbers	106
5.3.1	Effect of the Mach number (I) (different IMF B_z)	107
5.3.2	Effect of the Mach number (II) (different densities)	115
5.3.3	Discussion	116
5.4	Wave propagation	117
5.4.1	Consequence of these two enhancements of E_y	125
5.5	Conclusion	126
VI. Exploring the Impact of Ionospheric Outflow on Magneto- spheric Dynamics		128
6.1	Introduction	128
6.2	Ionospheric outflow from different source regions	131
6.2.1	Methodology	131
6.2.2	Simulation results	135
6.3	Influence of outflow intensity	159
6.3.1	Methodology	159

6.3.2	Simulation results	160
6.4	Conclusion	169
VII.	Summary and conclusion	172
7.1	IMF southward turning	173
7.2	Solar wind density increase	173
7.3	Ionospheric heavy ions outflow	175
VIII.	Future work	176
8.1	A sudden increase in the solar wind velocity	176
8.2	Mass transport into the magnetosphere from the solar wind	177
8.3	Density dependence of the CPCP index	177
8.4	Effects of the ionospheric outflow velocity	177
8.5	Simulations of the real event	178
BIBLIOGRAPHY	179

LIST OF FIGURES

Figure

1.1	Panel a: Magnetic fields of a dipole in the presence of an infinitely conducting plane	2
1.2	Magnetic reconnection process.	4
1.3	The steady state of the magnetosphere with neutral point by Dessler (1968).	5
1.4	Schematic representation of different regions in the magnetosphere.	7
1.5	(a) International quiet solar year daytime ionospheric and atmospheric composition based on mass spectrometer measurements.	9
1.6	Panel a: Schematic representation of magnetospheric and ionospheric convection under southward IMF conditions.	12
1.7	Schematic diagram of different particle precipitation regions in the auroral oval for southward IMF (from <i>Akasofu</i> (1976)).	13
1.8	The projection of field-aligned currents in the ionosphere polar region	14
1.9	The schematic diagram of various causes of the ionospheric outflow (<i>Schunk and Sojka</i> (1997)).	16
1.10	Possible sequence of events involved in an isolated substorm viewed from noon-midnight cross section	18
2.1	The components of the Space Weather Modeling Framework	27
2.2	Exchange of information among GM/BATS-R-US, IM/RCM, and IE models.	28
2.3	Two neighboring blocks with the top block refined into 8 blocks.	32

3.1	Ionospheric potential patterns, with color contours representing the potential, and the arrows indicating the convection velocities.	44
3.2	Cross polar cap potential profile (top) and residual cross polar cap potential (bottom) obtained by removing an averaged undisturbed pattern (bottom).	45
3.3	Upper: the upstream position of the IMF transition on the Sun-Earth line as a function of time	48
3.4	Snapshots of the northern hemispheric magnetosphere in x-z plane: density	50
3.5	Snapshots of the northern hemispheric magnetosphere in x-z plane: electric field	52
3.6	The H component of ground magnetic field perturbations at various local times and latitudes	54
4.1	Cross polar cap potential as a function of time when the high dynamic pressure solar wind hits the bow shock around 17:20 UT with northward IMF conditions.	66
4.2	Residual potential patterns in the northern hemisphere after the dynamic pressure enhancement hits the magnetosphere under southward IMF conditions.	68
4.3	Continued.	69
4.4	Residual field-aligned current patterns in the northern hemisphere after the dynamic pressure enhancement hits the magnetosphere with southward IMF conditions.	71
4.5	The H component of the ground magnetic perturbations in the northern hemisphere at six different longitudes (six panels) at various latitudes (six panels) at various latitudes (six lines in each panel).	73
4.6	Upper row: electric fields on equatorial plane.	76
4.7	The current flow in a 3D view in the first phase.	77
4.8	Magnetospheric convection on the equatorial plane	81

4.9	Northward IMF condition: left column displays the plasma convection (shown by the black streamlines) in the equatorial plane, and the color contour is $\frac{d\Omega_{\parallel}}{dt}$ (calculated from the l.h.s of equation 4.1)	82
4.10	Southward IMF condition: left column shows the plasma convection (streamlines) in the equatorial plane, with the contour representing $\mathbf{J} \cdot \mathbf{E}$	85
5.1	One example from the “two-phase” group of the responses observed from the ground, the ionosphere and the magnetosphere due to the sudden solar wind density increase at Jan 04, 2001	96
5.2	Panel (a) shows ground-based observation about magnetic perturbations in the morning side above 50° of magnetic latitude, and the lines are in a order according to the latitudes.	97
5.3	The ionospheric response in the AMIE electric potential pattern.	98
5.4	One example from “single-phase” group of disturbances observed from the ground, the ionosphere and the magnetosphere due to the sudden solar wind density increase at 16:46 May 11, 2002.	99
5.5	Panel (a) shows the ground-based magnetic perturbations in the post-noon side, and Panel (b) shows magnetic field data from GOES.	100
5.6	The residual electric potential obtained by subtracting the base potential pattern, an average of potential patterns from 16:42 to 16:44, from the other patterns.	101
5.7	Superposed epoch results for “two-phase” group for northward (left) and southward (right) IMF cases.	102
5.8	Histogram of events that show two-phase responses and single-phase response to the sudden solar wind density increase as a function of different factors	103
5.9	From idealized simulations, the cross polar cap potential reacts to the same solar wind density change from $N = 5cm^{-3}$ to $N = 20cm^{-3}$ with different solar wind Alfvén Mach number.	108
5.10	The left panel (12 circles) shows the residual field-aligned current on the northern ionosphere after the sudden solar wind density enhancement encounters the bow shock.	111

5.11	The CPCP index (solid), the maximum positive potential (dotted), and the absolute value of the minimum negative potential (dashed) in two simulations	112
5.12	The northward magnetic perturbations at various latitudes along the 15 MLT longitude from two simulations	114
5.13	The CPCP from simulations with the same IMF B_z but different solar wind densities.	115
5.14	Results from two idealized simulations (Mach number = 8.0 and 2.0)	119
5.15	The duskward inductive electric fields at $7 R_e$ on the Sun-Earth line as a function of time, for different Mach number simulations.	121
5.16	The solar wind density, dynamic pressure, electric field (y component), Alfvén Mach number, Bow shock position, and the SYM-H index for the June 02, 2007 event.	123
5.17	The duskward electric field observed by electric field instrument on board the THEMIS C spacecraft on June 2, 2007 when the spacecraft was orbiting within the dayside magnetosphere	124
6.1	The grid setup in the outflow simulations A and B, viewed from the noon-midnight meridian plane.	132
6.2	The artificial ionospheric outflow specified at the inner boundary of the MHD model BATS-R-US for two simulations.	134
6.3	The evolution of ionospheric O^+ outflow from the dayside cusp region starting at 03:00.	137
6.4	The evolution of ionospheric O^+ outflow from the nightside auroral region starting at 03:00.	138
6.5	The CPCP index, tail X-line position, earthward ejection speed on the earthside of X-line, and the D_{st} index for Simulation A (solid) and B (dashed).	139
6.6	The evolution of the ring current (banana shape) in the equatorial plane after 04:00 in Simulation A where the ionospheric outflow is originated from the cusp region.	141
6.7	Left panel: The position of the subsolar dayside magnetopause as a function of time.	142

6.8	Local reconnection rate (top) and global reconnection rate (bottom) for Simulation a (solid) and b (dashed).	145
6.9	The mass density for total (solid), H^+ (dashed), O^+ (dash-dot) ions, and magnetic field (blue) in the magnetospheric side of the subsolar magnetopause in Simulation A.	146
6.10	Plasma density in the dayside magnetosphere on the equatorial plane at two different times.	147
6.11	The energy density (solid, left label) and particle energy (dashed, right label) along a streamline (top panel) of ionospheric cusp heavy ions.	153
6.12	The same format as in Figure 6.11, but this is from Simulation B (night side auroral outflow).	154
6.13	Dst^* index (solid) calculated from the DPS relation (Equation 6.6	161
6.14	Top panel: the Z component magnetic field in the equation plane for the dusk side at time 03:15UT.	162
6.15	The shear velocity and the threshold of Kelvin-Helmholtz instability across the magnetopause boundary on the line of (7,6,0) to (10,10,0) R_e as a function of simulation time	165
6.16	Contour of the difference between the left and right hand sides of Equation 6.8 with angles range from 0 to 90° (i.e., parallel to perpendicular propagation of the waves with respect to the equatorial magnetopause).	168
6.17	The cross polar cap potential index for two simulations with outflow density of 20 cm^{-3} (solid) and 40 cm^{-3} (dashed) respectively.	169

ABSTRACT

The terrestrial environment is controlled by many external factors, some of which can potentially drive strong geomagnetic storms. In this dissertation, how the terrestrial magnetosphere-ionosphere (MI) system responds to solar wind variations and the subsequent self-modulation within the MI system are investigated by utilizing the Space Weather Modeling Framework (SWMF).

Studies of an interplanetary magnetic field (IMF) southward turning demonstrate that the arrival of the IMF discontinuity at the bow shock does not immediately disturb the ionosphere. With a solar wind speed of 400 km/s , the delay is about 10 minutes later. In addition, we find that a sudden increase in the solar wind density produces a two-phase response observed in ground-based magnetic perturbations and ionospheric potentials. The two phases are ascribed to the emergence of two successive pairs of field-aligned currents (FACs), which are caused respectively by dusk-to-dawn inductive electric fields due to a sudden compression of the magnetosphere and by magnetospheric vortices associated with the high-pressure gradient under northward IMF conditions or associated with large shear flows under southward IMF conditions. Although actual observations suggest that not all the solar wind density increase events are associated with a two-phase pattern, numerical simulations confirm the existence of the two-phase response. In addition to the two-phase response, the sudden compression launches Earthward-propagating waves that are further reflected multiple times between the Earth and magnetopause boundaries, resulting in multiple sets of the two-phase response.

Although the solar wind variations create disturbances in the MI system, one of the

self-modulation processes within the MI system, the ionospheric heavy ion outflow into the magnetosphere, is equally important. The dayside cusp-origin heavy ion outflow significantly disturbs the magnetotail and provides significant energy to the ring current; while direct leakage of the heavy ions into the inner magnetosphere from the nightside aurora provides little geomagnetic feedback. Sufficient mass loading into the magnetosphere can lower the threshold of the Kelvin-Helmholtz instability, triggering surface waves more easily near the equatorial magnetopause boundary, changing the efficiency of the solar wind-magnetosphere coupling.

CHAPTER I

Introduction

The “Solar Wind” was first named by Eugene Parker describing the supersonic flow of particles out of the Sun. This stream of fully ionized plasma consists primarily of hot electrons and protons with a minor fraction of helium ions. The wind originates primarily from coronal holes that occur predominantly near the Sun’s poles (*Hundhausen (1977)*). The expanding solar wind fills interplanetary space, carrying the solar magnetic field lines, embedded in the plasma, to form the interplanetary magnetic field (IMF). Beyond 15-20 solar radii, the solar magnetic field is dominated by the solar wind flow which expands radially away from the Sun. However, due to the solar rotation and the anchoring of the open field line to the Sun, a spiral-shape IMF (*Parker (1958)*) is formed. At the orbit of the Earth, one astronomical unit (AU) from the Sun, the IMF has an average angle of $\sim 45^\circ$ to the radial direction (*Hundhausen (1995)*). The solar wind speed at 1 AU ranges from 300-800 $km s^{-1}$ (*Gosling (1971)*) and the density of the solar wind varies from 1-80 cm^3 .

1.1 Solar wind-magnetosphere coupling

The interaction of the solar wind with a planet’s such as Earth’s magnetic field gives rise to a magnetosphere. The Earth’s field is generated by the currents flowing in the Earth’s core and is mostly dipolar if it is not impacted by external forces. The

Earth itself is largely protected from the solar wind by the magnetosphere, which deflects most of the solar energetic particles, causing the particles to travel around the boundary of the magnetosphere rather than bombarding the Earth's atmosphere or surface.

One of the early models of the solar wind-magnetosphere interaction was proposed by *Chapman and Ferraro* (1930, 1931, 1932). The principal feature of the model was a transient outflow of ionized gas from the Sun consisting of positive ions and electrons but having no net charge. Figure 1.1(a) illustrates the interaction between the Earth's dipolar magnetic fields and the solar wind plasma in the case of an advancing infinite planar front. This is mathematically equivalent to the creation of an equal and parallel dipole moment, at a distance behind the front the same as the distance that the Earth's dipole is ahead of the front.

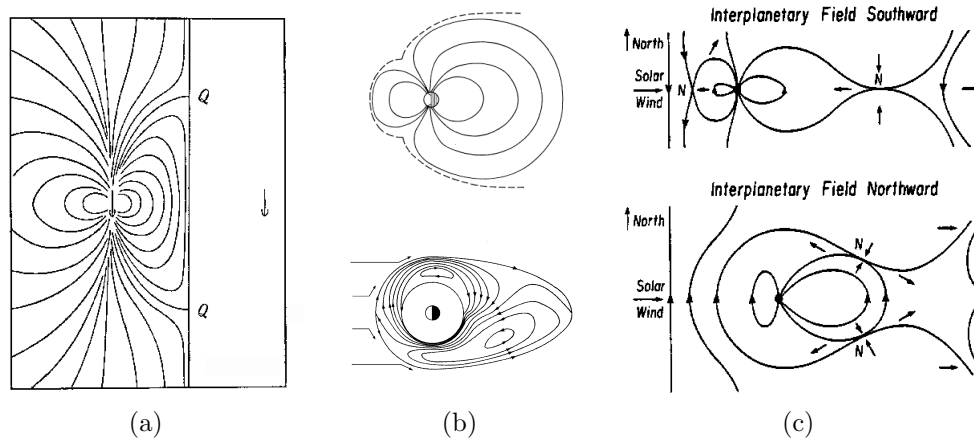


Figure 1.1: Panel a: Magnetic fields of a dipole in the presence of an infinitely conducting plane. The strength of the magnetic field goes to zero in the region labeled by Q (*Chapman and Bartels* (1940)). Panel b: The closed magnetosphere as a result of viscous interaction with the solar wind in the noon-midnight meridian (top) and on the equatorial plane (bottom) [*Axford and Hines* (1961)]. Panel c: The configuration of the magnetosphere under southward (top) and northward (bottom) IMF conditions [*Dungey* (1961)].

Later, *Axford and Hines* (1961) introduced the concept of viscous interaction between the solar wind and the magnetosphere, as shown schematically by the closed magnetosphere model in Figure 1.1(b). The top plot shows a noon-midnight meridian

cut of the magnetosphere, in which each magnetic field line is closed in the ionosphere. As a consequence of viscous interaction, the outside boundary of the magnetosphere and the magnetically connected high-latitude ionosphere undergo an antisunward plasma convection as dragged by the solar wind flow, while the plasma convection inside of the magnetosphere and in the low-latitude ionosphere is sunward because the circulation must be closed in this closed magnetosphere model. Under the superposition of the Earth rotation, the above circuit of plasma convection turns to an asymmetric pattern as illustrated in the bottom plot.

These early models of solar wind-magnetosphere coupling, however, ignored the important role of the interplanetary magnetic field (IMF) that is embedded in the solar wind. The interaction of magnetic field lines from two different plasma domains may locally result in topology changes, in which the existing magnetic field lines are cut and the free ends are reconnected to other field lines (Figure 1.2). This process is called “magnetic reconnection” (*Dungey (1953); Sweet (1958); Parker (1957)*). It favors regions where the magnetic field lines in two different domains have opposite orientations that can transform magnetic to kinetic components of the total energy. The macroscopic motion of the plasma is also influenced during reconnection. Before reconnection, the plasma moves perpendicular to the field lines towards the diffusion region in the middle (orange region in Figure 1.2), as pointed by the red arrows; after reconnection, the plasma is expelled in the direction of the original orientation of the magnetic field lines. The middle of the diffusion region, where the magnetic field is null, is called a “neutral point” or X-point. While the term reconnection is for descriptive purpose of the topology change only, the actual mechanism is associated with resistivity according to resistive magnetohydrodynamics (MHD) theory. The reconnection occurs because the plasma electric resistivity near the boundary layer that separates the two magnetic domains opposes the currents necessary to sustain the change in the magnetic field. The resistivity of the current layer allows the magnetic

flux from either side to diffuse through the current layer and cancel the flux from the other side. In this case, the plasma is pulled out by magnetic tension along the direction of the magnetic field lines. The resulting decrease in the pressure in the diffusion region pulls more plasma and magnetic flux into it, yielding a self-sustaining process.

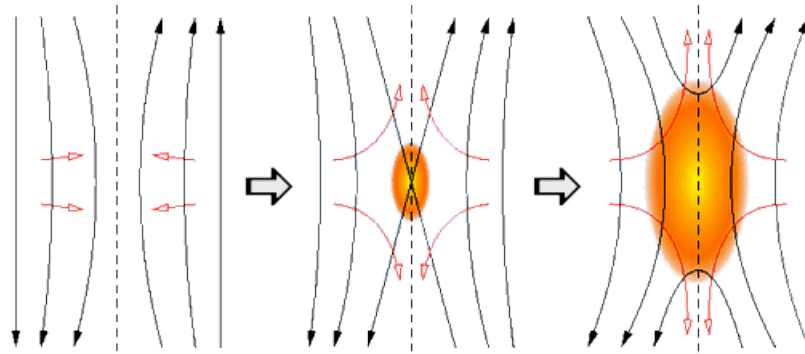


Figure 1.2: Magnetic reconnection process. Black lines are the magnetic field lines, red arrows represent the plasma flow, and the orange region is the diffusion region.

Such magnetic reconnection was first applied to magnetospheric physics by *Dungey* (1961), who attributed the momentum transfer from the solar wind to the magnetosphere to the magnetic reconnection between the IMF and Earth intrinsic magnetic field. His proposed magnetosphere configurations with different IMF orientations are shown in Figure 1.1(c). Under southward IMF conditions, the model predicts two reconnection points where the interplanetary magnetic field lines merge with the geomagnetic field lines: one is in the front of the magnetosphere, and the other one is in the tail. The reconnection first occurs near the subsolar point of the magnetosphere, and the outermost originally closed field lines turn into open field lines with the foot of these field lines located in the Earth polar region. The newly opened field lines then convect antisunward, inducing electric fields that are transmitted into the ionosphere. These open field lines are then reconnected in the stretched geomagnetic tail again, creating newly closed field lines, which flow towards and around the Earth, balancing the earlier eroded magnetic flux by the dayside reconnection. On the other

hand, with northward directed IMF, no subsolar reconnection takes place. Instead, the reconnection occurs at higher latitudes in the poleward of the cusp region between the diverted IMF around the magnetosphere and the tail lobe intrinsic field. In this case, the tail magnetic fields are more dipolar compared to the stretched magnetotail in the southward case and no tail reconnection occurs in the equatorial plane.

Axford et al. (1965) suggested an open magnetospheric model resembling that of *Dungey* (1961) but more closely approximating the correct scale. In this model, the flow in the tail enters into a neutral line, a separatrix of the magnetic field lines in the tail. There is a neutral sheet Earthward of the neutral line, which is embedded in the plasma sheet. *Dessler and Juday* (1965) postulated that a true neutral sheet exists with no flux crossing this plane, and the tail is essentially infinite. In their model, the bow shock was for the first time predicted in the interaction between the supersonic solar wind and the magnetosphere. *Dessler* (1968) updated his model by combining the open tail model with the neutral line model, as illustrated in Figure 1.3.

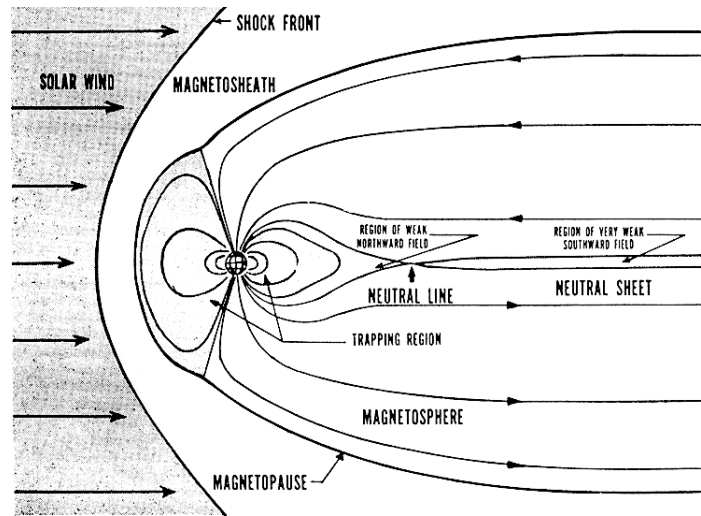


Figure 1.3: The steady state of the magnetosphere with neutral point by Dessler (1968).

The well-accepted structure of the magnetosphere is to date shown in Figure 1.4. As the flow around the Earth is supersonic and superalfvénic, a *bow shock* wave is formed ahead of the Earth. The shock slows down the solar wind so that the flow

is diverted around the Earth. A tangential discontinuity called the *magnetopause* (*Chapman and Ferraro (1931)*) separates the shocked solar wind from the region dominated by the terrestrial magnetic dipolar field. The region between the bow shock and the magnetopause is called the *magnetosheath*. In contrast to the compressed dayside magnetosphere, the magnetic field lines on the nightside are stretched in the flow direction, forming the *magnetotail* (see *Ness (1987)*). The *polar cusp* (*Vasyliunas (1979)*) lies near the interface between the dayside and nightside magnetosphere at polar latitudes. The plasma *mantle* (*Vasyliunas (1979)*) is located just antisunward of the cusp in a region of open magnetic field lines, with the magnetic foot point attached to the Earth and the other end in interplanetary space. The plasma flow in this region is primarily parallel to the magnetosheath flow with a small inward flow towards the neutral sheet. The density decreases from the magnetosheath value. The *plasma sheet* (*Pilipp and Morfill (1978)*) is located near the equator of the magnetosphere around the neutral sheet, and it contains dense and hot plasma. Between the plasma sheet and mantle is the *magnetotail lobe* (*Pilipp and Morfill (1978)*) region, where the plasma density is quite low compared to the surrounding regions. The magnetic field lines in the northern and southern lobes are directed in opposite directions. The boundary between the lobes and the plasmasheet is the *plasma sheet boundary layer* (PSBL) (*Vasyliunas (1979)*), which contains a mixture of plasma from the two regions. The *plasmasphere* (*Chappell (1972)*), which extends approximately from $3-7 R_e$ around the Earth in the closed field-line region, is populated with cold dense plasma and is dominated by corotation drift. Coexisting with the plasmasphere in this region are the *radiation belts* and *ring current*. The radiation belts contain charged particles of MeV energy, while the ring current, flowing in the westward direction around the planet, consists of charged particles with tens to hundreds of keV. At low latitudes near the equatorial plane, *low latitude boundary layer* (*Vasyliunas (1979)*) (LLBL) mixes the magnetosheath plasma with that in the magnetosphere.

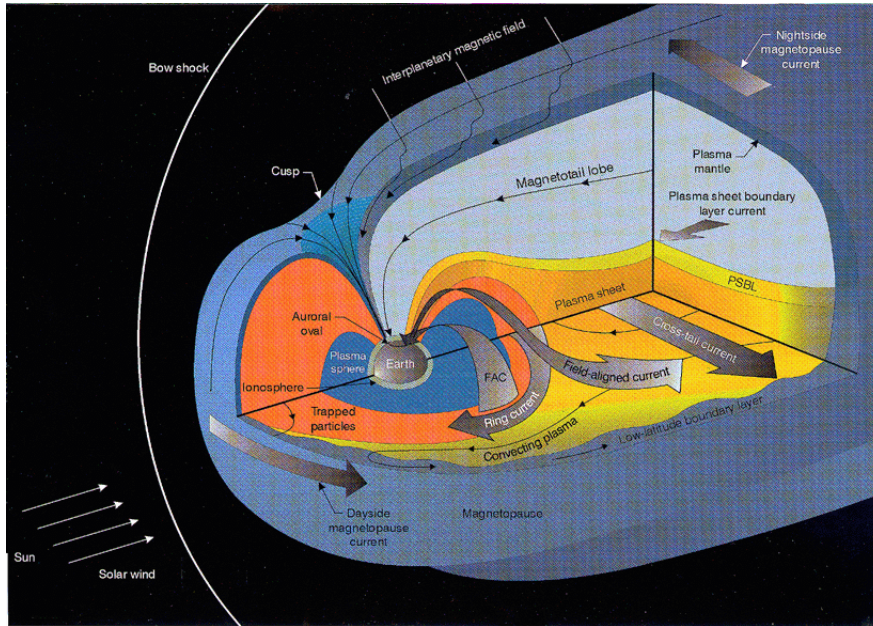


Figure 1.4: Schematic representation of different regions in the magnetosphere.

In the magnetosphere, there are several principal current systems that play important roles in the formation of the magnetosphere. The magnetopause current (*Chapman and Ferraro (1930, 1932)*), also called Chapman-Ferraro current, flows around the magnetopause. It separates the terrestrial magnetic field from the IMF. The tail current flows near the equator of the magnetosphere, separating the northern and southern lobe region magnetic field lines that are directed in opposite directions. It flows across the neutral sheet in the dawn-to-dusk direction and closes through the top and bottom boundaries of the magnetotail. The ring current (*Kozyra and Liemohn (2003)*), generally located between 3 and 6 R_e , contains charged particles of 10-200 keV that are generally trapped by the closed field lines. These particles convect in the near-Earth region where the gradient-curvature drift is the dominant driver. Hence, the ring current flows westward since the positive ions drift westward while electrons drift eastward. The field-aligned currents (FACs), also called Birke-land current, flows along the magnetic field lines into or out of the ionosphere (*Iijima and Potemra (1978)*).

1.2 Magnetosphere-ionosphere coupling

The energy deposited from the solar wind is mostly dissipated in the ionosphere, which is referred to as the energy “sink” in the terrestrial system. The ionosphere results from the partial ionization of the upper atmosphere of the Earth at altitudes of 60-1000 km by ultraviolet and X-ray solar radiation. The vertical structure of the ionosphere primarily consists of D, E, F (F1, F2) regions and topside ionosphere (Figure 1.5(a)). The breakdown of these regions is based on what wavelength of the solar radiation is absorbed in that region most frequently (*Luhmann (1995)*). The D layer is the innermost layer, extending from 60-90 km above the surface of the Earth. The primary source of ionization in this region is solar X-rays and Lyman- α ionization of the NO molecule. The ionized particles in this layer are dominated by molecular ions, negative ions and water cluster ions. The E layer is the middle layer, covering from 90 km to 150 km. It results from the soft X-ray and far ultraviolet radiation ionization of molecules and is composed of NO^+ , O_2^+ , and N_2^+ . The F region is ionized by extreme ultraviolet radiation and is usually divided into three subregions. The F1 layer is the lowest layer in the F region, covering from 150 to 200 km. It is photochemistry dominated, with the principal ions being O^+ and NO^+ . The important reactions in this region are photoionization of neutral atomic oxygen and loss in reaction with N_2 and O_2 . The F2 layer extends from about 200 km to more than 500 km. It is a region where a transition from chemical to diffusion equilibrium dominance occurs and a region dominated by O^+ from photoionization of atomic oxygen. Its peak electron density occurs at the altitude where the diffusion and chemical processes are of equal importance. This peak is referred to as the F2 peak, above which the diffusion process dominates, and the O^+ density follows a diffusive equilibrium profile and decreases exponentially. The topside ionosphere is defined to be the region above the F2 peak where O^+ is the dominant ion; it extends from about 600 to 1500 km at mid-latitudes. The region above this, where H^+ becomes

dominant, is referred to as the protonosphere.

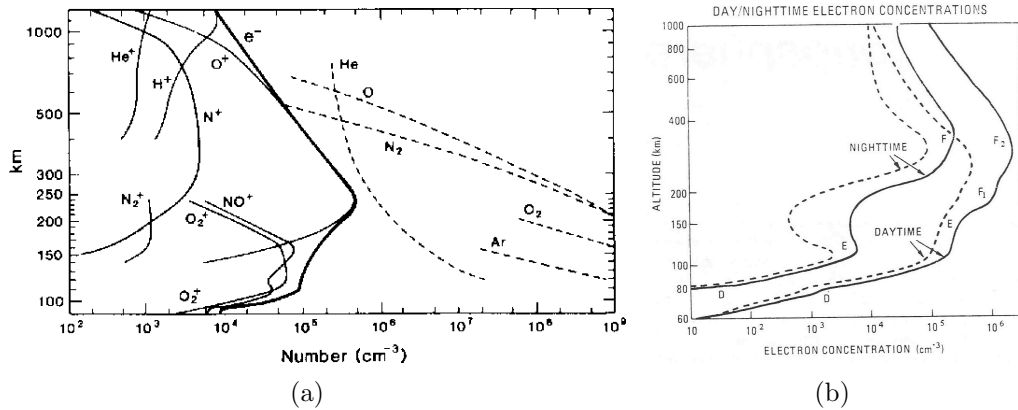


Figure 1.5: (a) International quiet solar year daytime ionospheric and atmospheric composition based on mass spectrometer measurements (*Johnson (1969); Luhmann (1995)*). (b) Typical ionospheric density profiles for the day and night times during solar maximum (solid) and minimum (dashed) (*Tascione (1994)*).

While this vertical structure of the ionosphere is very typical during the day time, the ionosphere decays rapidly at night because the ionization sources - photoionization disappears, leaving the loss chemistry reactions (such as dissociative recombination) only. Due to a fast loss rate in the E region, it decays quickly; while the F region slowly decays in a shape-preserving fashion. The slow decay in the F region is associated with the small loss reaction rate in that region (*Schunk et al. (1976)*). However, this does not mean the ionosphere keeps decaying as time goes on, since ionization sources other than the direct photoionization indeed exist at night, potentially maintaining part of the nocturnal ionosphere (*Luhmann (1995)*). Figure 1.5 (b) shows a nighttime ionosphere condition, in which the F region is partially maintained by downward flow of ionization from the overlying plasmasphere as well as by equatorward meridian neutral wind from the dayside hemisphere inducing an upward plasma drift that raises the F layer and slows down the decay. There is a weak sporadic E layer in the night time profile, which results from the ionization enhancement in the E region and is dominated by long-lived metallic ions created by neutral metal atoms during meteor ablation (*Whitehead (1989)*).

The dense region of the ionosphere (E and F regions) contains substantial electrons and ions, leading to a highly conductive ionosphere, allowing currents flowing in the ionosphere. Above about 150 km, the conductivity is low due to few collisions in that region and the charged particles move at a bulk plasma-drift velocity $\mathbf{E} \times \mathbf{B}/B^2$. Below this altitude and above about 110 km, the ions can only complete part of the gyrocycle around a magnetic field line before they collide with the neutrals, leading to a diverted direction, while the electrons in this region are still in the $\mathbf{E} \times \mathbf{B}$ direction due to their small electron-neutral collision frequency. Therefore, the diverted motion of the ions generate the Pedersen current, while the electrons create the Hall current. Below 110 km, even the electrons experience significant collisions with the neutrals, resulting in no currents in this region because both ions and electrons move roughly with the neutrals (*Carlson and Ggeland (1995)*).

1.2.1 High-latitude electromagnetic coupling

The ionosphere and magnetosphere are strongly electromagnetically coupled at high latitudes via processes such as motional electric fields, auroral particle precipitation, and field-aligned currents (FACs).

Motional electric fields

As the solar wind is a highly conducting, collisionless, and magnetized plasma, a steady bulk solar wind flow with velocity \mathbf{V}_{sw} (in Earth’s frame of reference) requires the existence of an electric field, satisfying the “ideal magnetohydrodynamic (MHD) condition” (*Walén (1947)*): $\mathbf{E} = -\mathbf{V}_{sw} \times \mathbf{B}$. Conversely, an electric field impressed on a magnetospheric plasma produces a bulk flow satisfying the above relation. One property of the relation is frozen-in theorem (*Alfvén (1942)*), i.e., any group of ions or electrons initially sharing a field line continue doing so. But the above relation is not valid when rapid time variation is important (*Kivelson and Russell (1995)*). In the Dungey model (*Dungey (1961)*), when the streaming solar wind pulls the open

field lines antisunward over the top/bottom of the magnetosphere, the plasma in a flux tube moving with the solar wind stream will sense a dawn-to-dusk directed electric field. In steady state, the electric field is sensed all along the flux tube as the field lines are perfectly conducting and therefore equipotential. This electric field, mapped down to the ionosphere along the field lines, drives antisunward plasma flows over the polar cap region according to the $\mathbf{E} \times \mathbf{B}$ drift. When the open field lines convect down towards the magnetotail and reconnect with the field lines from the other hemisphere, newly closed geomagnetic field lines are generated, returning magnetic flux towards the dayside around either dawn or dusk side of the Earth (*Hughes (1995)*). Correspondingly, the $\mathbf{E} \times \mathbf{B}$ drift in the ionosphere is in the sunward direction at lower latitudes, closing the flow circuit. This electromagnetic coupling between the ionosphere and the magnetosphere is shown in Figure 1.6(a). As a result of the electric field imposed over the polar cap and corresponding charges on the open-closed field line boundaries, electric potential over the high-latitude ionosphere displays a two-cell pattern, as shown in Figure 1.6(b) with positive potential on the morning sector and negative one in the afternoon sector. Such a pattern is typical for southward IMF conditions. The difference between the maximum and minimum potentials over the polar cap ionosphere is defined as the cross polar cap potential (CPCP) index, which is widely used as a measure of geomagnetic activity level.

Auroral precipitation

Geomagnetic field lines can guide energetic electrons and protons from the magnetosphere down to Earth's atmosphere. The precipitating particles collide with the upper atmosphere neutrals, exciting them to higher energy levels, leading to the emission of auroral light. Most such particle precipitation occurs in the auroral oval, which contains discrete aurora that form curtain or ray shapes that are often easily visible with the naked eye, and diffuse aurora, which are fainter and lack sharp spatial boundaries (*Newell (2003)*). The diffuse aurora is primarily caused by the precipitation of low-

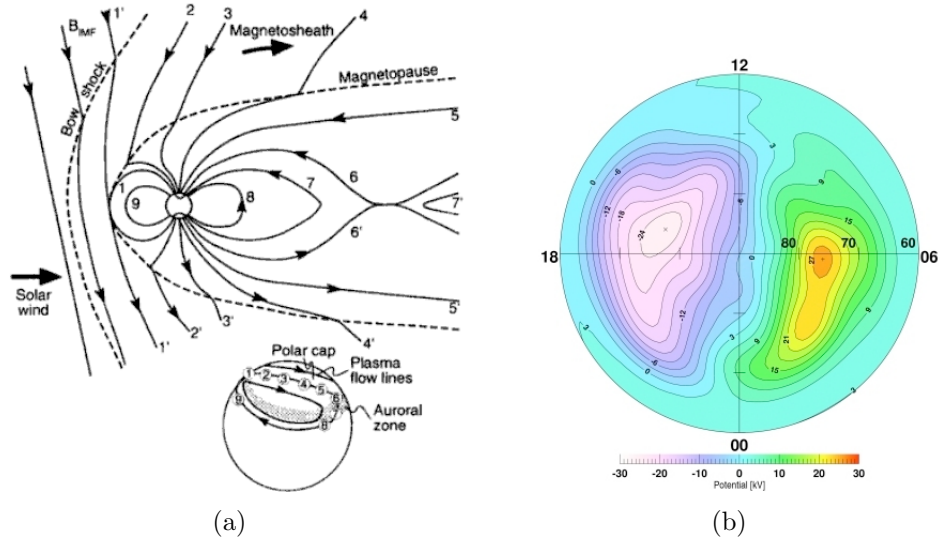


Figure 1.6: Panel a: Schematic representation of magnetospheric and ionospheric convection under southward IMF conditions (from *Hughes* (1995)). Panel b: Ionospheric electric potential pattern under southward IMF conditions (adapted from *Haaland et al.* (2007)).

energy electrons originating in the central plasma sheet (*Eather and Mende* (1971)), representing a direct dumping of various space plasma population surrounding the Earth, providing large energy source to the high-latitude upper atmosphere. The discrete aurora, however, is caused by strong field-aligned accelerated beams of electrons with energy up to hundreds of eV or occasionally tens of keV (*Newell et al.* (1996)). These high-energy electrons likely originate from magnetospheric boundary layers, such as LLBL, plasma sheet boundary layer, and field lines that thread the plasma mantle (*Newell et al.* (1992)). Figure 1.7 illustrates a schematic diagram for different particle precipitation regions in the auroral oval for southward IMF (*Akasofu* (1976)). In addition to the diffuse aurora (in shaded region) and discrete aurora (in lines) that are the major precipitation representatives, there is other particle precipitation which contributes much smaller energy flux, such as low-energy polar rain precipitation in the polar cap, soft precipitation in the cusp, and diffuse auroral patches in the morning oval.

Field-aligned currents

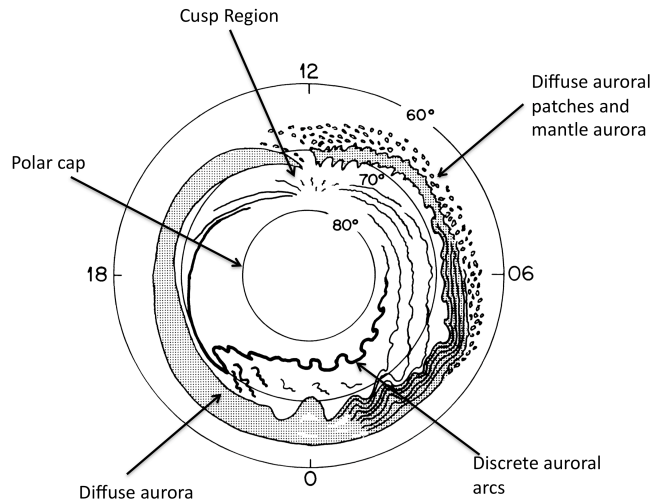


Figure 1.7: Schematic diagram of different particle precipitation regions in the auroral oval for southward IMF (from *Akasofu (1976)*).

The key electrodynamic element in the magnetosphere-ionosphere coupling is field-aligned currents flowing between the two regions along magnetic field lines, as they provide a bridge for the two systems to exchange mass, momentum, and energy. *Iijima and Potemra (1976a,b)* determined two FAC systems over the polar cap region: region-1 and region-2 FACs, after statistically studying the characteristics of large-scale field-aligned currents using magnetometer data. The projection of the averaged FACs in the ionosphere is illustrated in Figure 1.8, as adapted from *Iijima and Potemra (1978)*. The region-1 FAC flows down into the dawnside ionosphere at the poleward edge of the auroral zone and flows away from the duskside ionosphere as a returning region-1 FAC. These FACs are closed in the ionosphere by the horizontal Pedersen current and are connected far out in the magnetosphere to the boundary layers and the plasma sheet (*Tsyganenko et al. (1993)*). Equatorward auroral oval is another oppositely directed set of currents called region-2 FACs, which connect the westward partial ring current in the inner magnetosphere with the ionosphere (*Vasyliunas (1970)*) and flow into the ionosphere on the duskside and up from the

ionosphere on the dawnside. Both systems display curved shapes, covering a wide range of local time. While this is a typical pattern for southward IMF condition, during northward IMF, an additional FAC system appears poleward of the region-1 system called NBZ current system (*Iijima et al. (1984)*), which is generally much smaller in spatial extent than the other two FAC systems and in opposite direction to the region-1 FACs at a given local time. The NBZ current is connected to the sunlit side and increases as the magnitude of B_z increases.

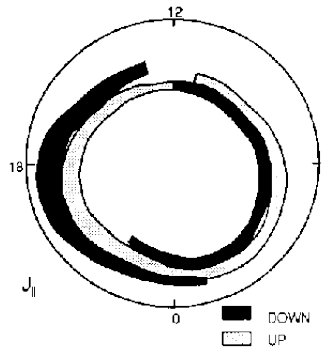


Figure 1.8: The projection of field-aligned currents in the ionosphere polar region. The inner pair is Region-1 FAC system, and the equatorward pair is Region-2 FAC system. Black represents a downward flowing current, and white stands for an upward flowing current (from *Iijima and Potemra (1978)*).

The above high-latitude electric field in ionosphere-magnetosphere coupling can be modified by neutral winds (*Ridley et al. (2003)*, *Lu et al. (1995)*), which result from the neutral-ion coupling in the thermosphere. The neutral-ion coupling occurs through collisions, which cause the neutrals to be accelerated towards the ion velocity but with a time lag of a few hours due to the inertia of the neutrals. In turn, the neutrals can generate electric fields that lead the ions to move with the neutrals. Therefore, when the magnetospheric dynamo source of the electric field is suddenly weakened, the inertia of the neutrals can help maintain the ion convection. This is known as the fly-wheel effect (e.g., *Richmond (1995)*). The inclusion of the neutral winds has been found to reduce the joule heating by as much as 28% and drive field-aligned currents as much as 27% of the magnetospheric generated FACs (*Lu et al.*

(1995)). The neutral winds can also increase the electric potential in the ionosphere during southward IMF times (*Ridley et al. (2003)*), and causes pressure changes in the magnetosphere (*Ridley et al. (2003)*, *Peymirat et al. (1998, 2002)*).

1.2.2 High-latitude mass coupling

In addition to the above electromagnetic couplings via convection electric fields, FACs, and energetic particle precipitation, the magnetosphere and ionosphere are also highly linked through ionospheric ion outflow (*Dessler and Michel (1966)*). These particles escape into the magnetosphere and populate various magnetospheric boundary layers and plasma regions, influencing the magnetospheric properties and dynamics. For detailed review on the ionospheric plasma outflow, *Schunk and Sojka (1997)*, *Yau and Andre (1997)*, *Andre and Yau (1997)*, *Ganguli (1996)*, and *Schunk (2000)* have provided plenty of information about the theoretical, observational, and numerical development on the ionospheric outflow.

The ionospheric outflow plasma, primarily composed of heavy ions O^+ and light ions such as H^+ and He^+ , can be categorized into two groups according to the outflow mechanism: classic outflow and energetic outflow. The classical outflow includes the polar wind outflow and auroral bulk outflow. The polar wind is a bulk H^+ ion outflow which occurs throughout the entire polar region, starts at an altitude of 1000 km, and has a typical velocity of 1 km s^{-1} at an altitude of about 2000 km. It is generally driven by a thermal pressure gradient in the F-region and ambipolar electric fields arising from the charge separation between the light electrons and heavy ions. Typically, the plasma pressure and ambipolar electric field are sufficient to drive the light thermal ions up to escape the ionosphere, but not heavy ions. The auroral bulk outflow, occurring on both dayside and nightside auroral regions, is dominated by O^+ starting from an altitude of about 400 km or higher at velocities up to about 1 km s^{-1} . It is likely driven by frictional heating of O^+ in the collision dominated ionosphere or by

increased electron temperature in the auroral electron precipitation region. But most ions cannot escape unless they are further energized by other acceleration mechanisms along their way upward, as described below.

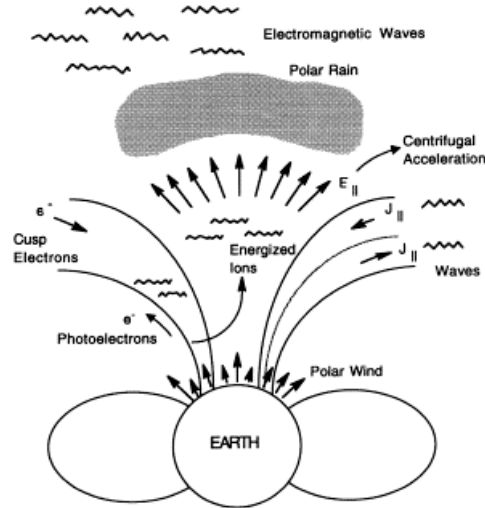


Figure 1.9: The schematic diagram of various causes of the ionospheric outflow (*Schunk and Sojka (1997)*).

The other category is energetic ion outflow, also called non-classical polar wind outflow (*Schunk and Sojka (1997)*). These superthermal and energetic outflow ions include ion conics and ion beams. The ion conics, observed by rockets at altitudes of a few hundred kilometers, occur both on the dayside and nightside. They are accelerated by perpendicular electric fields oscillating within some frequency range over an extended altitude region. The ion beams travel along the magnetic field lines, and primarily occur above 500 km. They are driven by parallel electric fields, and by magnetic pitch-angle folding of some upward moving conics. They may be gradually energized in the perpendicular direction to achieve a conical shape and then are $\mathbf{E} \times \mathbf{B}$ convected towards the night side. These two types of energetic ion outflow are also possibly driven by photoelectron drag, centrifugal acceleration, hot magnetospheric particles, and wave-particle interactions, as illustrated in Figure 1.9. For instance, in sunlit regions, escaping photoelectrons can accelerate and drag the iono-

spheric ions up; the centrifugal force will increase the ion velocity; the precipitating magnetospheric electrons will energize the ionospheric ions.

1.3 Magnetic storms and substorms

The magnetosphere-ionosphere system is a highly dynamic system that undergoes a sequence of changes each time the IMF turns southward. These sequences are categorized into geomagnetic storms or substorms, during which the energy and plasma distribution within the system is rapidly and significantly altered. Magnetospheric storms are large, prolonged disturbances of the magnetosphere, resulting from a chain of causative events originating from the Sun such as coronal mass ejection (CME) (*Zhang et al. (2007)*). Fast CME originates from the solar closed field-line region and drives a shock front with compressed ambient plasma and discontinuity behind it (*Bame et al. (1979)*), carrying large nonrecurring interplanetary variations of plasma density and magnetic field towards the Earth. The magnetic storm usually lasts for a few days and consists of several phases: *sudden commencement*, *main phase*, and *recovery phase* (*Akasofu (1964)*). The *sudden commencement* is commonly associated with an impulsive interplanetary shock that compresses the magnetosphere. The *main phase* of a magnetic storm is usually caused by extended periods of large southward IMF which allows large dayside reconnection and amplifies the transfer of magnetic energy and penetration of electric field into the magnetosphere, increasing a large amount of particles injected into the ring current. The increased ring current induces a southward magnetic field in the center of the Earth, depressing the surface magnetic fields. These decreases, measured by the D_{st} index, can reach hundreds of nanotesla during strong storm periods. The main phase is the time period when the ring current increases and the horizontal magnetic field decreases. It can typically last from a few hours to about a day. The *recovery phase* occurs when the southward component of the IMF weakens or disappears. The decreased dayside reconnection

rate weakens the electric field penetrating into the magnetosphere, resulting in less energetic particles being ejected into the ring current. Instead, low-energy plasma starts to refill the plasma sheet, contributing little ring current. Therefore, the ring current starts to decay and the horizontal magnetic field starts to return to its normal level. Many storm recoveries occur in two stages: the first rapid recovery results from the fast loss of heavy ions and the second gradual recovery from the slower loss of protons. The recovery phase may last for several days.

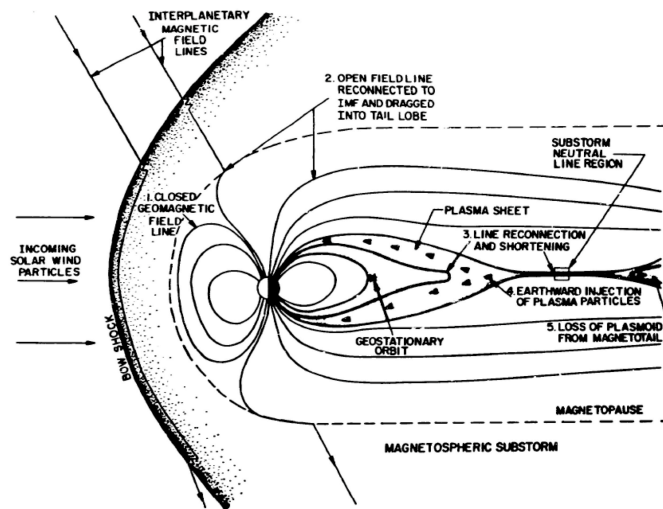


Figure 1.10: Possible sequence of events involved in an isolated substorm viewed from noon-midnight cross section. (from *Baker and Belian* (1986)).

In addition to the above long-lasting magnetic storms, relatively short-lasting disturbances are caused by substorms that are usually responsible for the aurora. In an idealized circumstance, isolated substorms are generated by brief periods of southward IMF (*Baker and Belian* (1986)). While the sequence of changes in a substorm is still under debate, one possible sequence of an isolated substorm was reviewed by *McPherron* (1979) and is interpreted in Figure 1.10 (from *Baker and Belian* (1986)). Northward IMF minimizes the dayside reconnection and hence small amount of magnetic flux is transferred into the geomagnetic tail. Southward IMF,

however, substantially increases the dayside reconnection rate (*McPherron (1979)*) and allows more magnetic flux to be convected into the magnetotail, increasing the magnetic stress on the tail, leading to a thinning of the plasma sheet and to tail magnetic reconnection. The process of storing magnetic energy in the tail is called the *growth phase*. Once the tail becomes unstable due to too much accumulative magnetic energy, it suddenly releases the energy, marking the time of *substorm onset* and the beginning of *substorm expansion phase*. The plasma flow out of reconnection region is toward the Earth on the near-Earth side of the x-line and away from the Earth on the other side. At substorm onset time, the ejection of hot plasma into the Earth's upper atmosphere results in a sudden brightening of a portion of equatorward auroral arcs in the pre-midnight sector, while during the expansion phase, the brightening expands rapidly westward and poleward, significantly disturbing the magnetic and current distribution in the auroral oval and developing a westward auroral electrojet. At the end of the expansion phase, auroral activity begins to dim at lower latitudes of the oval and the westward electrojet starts to cease, indicating the *substorm recovery phase*. The termination of the highly active auroral oval is due to the northward IMF turning which significantly reduces magnetic flux into the magnetotail and energy precipitation down to the ionosphere.

1.4 Motivation

The magnetosphere is almost continuously undergoing significant changes, because the configuration and state of the magnetosphere are highly controlled by the ever-changing solar wind and IMF conditions. The solar wind pressure and the interplanetary magnetic field (IMF) will increase or decrease depending on the Sun's activity. The solar wind pressure changes modify the currents in the ionosphere, and the IMF interaction with the Earth's magnetic field causes the entire structure to evolve. Therefore, large changes in the solar wind and IMF are responsible for

the subsequent significant disturbances in the terrestrial system, such as geomagnetic storms.

1.4.1 Space weather prediction

Geomagnetic storms tend to cause rapid changes in the magnetospheric magnetic field. A time-varying magnetic field external to the Earth induces electric currents beneath the ground, which further creates secondary internal magnetic fields. According to Faraday's law of induction, an electric field at the surface of the Earth is induced associated with time variations of the magnetic field. The surface electric field generates currents, known as geomagnetic induced currents (GIC), to flow in any conducting structure. A sufficiently large current, caused by a geomagnetic storm, flowing in equipment that is susceptible to certain damage could eventually cause hazards (*Boteler et al. (1998); Kappenman (2004)*) by disrupting the normal operation of long electrical conductor systems, such as the electric transmission grid, buried oil and gas pipelines, and undersea communication cables. Magnetic storms also result in significant energization of the near-Earth radiation environment. The high-energy particles penetrating into the magnetosphere can damage electronics on board spacecraft through induced electric currents and also threaten the life of astronauts. These disturbances in the terrestrial system are called "space weather". It is therefore very important for the space environment community to forecast timings, based on observations of the solar conditions or the conditions at the upstream Langerian point, therefore providing space weather forecasts and warnings to the nation and the world. The forecasting timings include, for example, when the solar wind variations would arrive at the Earth's bow shock and when they may drive strong disturbances on the ground. One important driver of space weather is the sudden southward turning of the IMF orientation, because such IMF change typically corresponds to a transition from a quiet magnetosphere to a disturbed one. This dissertation will study the re-

sponse to this southward turning in order to quantify the time needed for the new IMF orientation to initialize disturbances in the ionosphere since its encounter with the bow shock.

1.4.2 Importance of the solar wind density

Another common solar wind variation involved in geomagnetic storms is the change in the solar wind density, which further changes the solar wind dynamic pressure. While the solar wind pressure can determine the size of the magnetosphere, less is understood about how the pressure influences the electrodynamics of the magnetosphere-ionosphere system. Many studies (e.g., *Gonzalez (1990)*; *Weimer (1995)*; *Boyle et al. (1997)*) have shown that the solar wind density has little to no effect on the electric potential in the ionosphere, different than the velocity that can help to control the electric potential. Recently, it has been suggested that the solar wind pressure helps to control the energy transfer from the solar wind to the ionosphere (*Lopez et al. (2004)*; *Boudouridis et al. (2003)*) and whether the ionospheric potential will be saturated (*Siscoe et al. (2002)*). While the role of the relatively calm solar wind density is questionable in driving the magnetosphere, transient or step changes in the density appear to have a strong influence on the magnetosphere for a short period of time (e.g., *Sibeck et al. (1989)*). Therefore, it is one of the tasks in this dissertation to understand the responses of the geospace system that occur promptly and last for a short time.

1.4.3 The impact of ionospheric outflow

In addition to its significant influence on the integrated MI system through “space weather” disturbances, solar wind variations impinging on the magnetosphere system also result in so called “self-modulating” responses within the integrated MI system. They occur when the system adjusts to the external and the resultant internal dis-

turbances, as the MI system needs to dissipate the excessive energy from the strong external driving. One such self-modulating process is an increasing outflow of heavy ions from the ionosphere into the magnetosphere. It is now generally accepted that the ionospheric ions are a significant source of magnetospheric plasma and that these ions play an important role in magnetospheric physics.

It is known that two main pathways exist for the ionospheric heavy ions entering into the plasma sheet, which serves as an important particle source for the ring current. The cleft ion fountain (*Lockwood et al. (1985)*) is a persistent but not dominant source of ionospheric outflow during solar minimum quiet time (*Peterson et al. (2006)*). *Elliott et al. (2007)* analyzed the TIDE measurements on board the Polar spacecraft, investigating the O^+ transport out from the cleft region. They concluded that the O^+ ions emanating from the cleft transport across the polar cap and have access to the ring current. Another pathway for the ionospheric heavy ions into the plasma sheet is to directly escape out of the nocturnal auroral oval, which generates energetic and large fluxes of O^+ outflow during storm times (*Tung et al. (2001)*). The auroral O^+ flows along auroral magnetic field lines into the magnetosphere, providing a fast pathway to the plasma sheet (*Daglis and Axford (1996)*).

A common scenario from previous studies is that during highly disturbed times, the ionospheric-origin heavy ions inside the magnetosphere undergo dramatic enhancements in number and energy densities and possibly exceed that of protons. *Ebihara et al. (2006)* examined the fate of the ionospheric ions inside the magnetosphere using a full-particle tracing scheme and found that most of the ionospheric outflowing ions arrive at the ring current, and the number of ions increases with the activity level. *Kistler et al. (2006)* statistically studied the O^+ density in both storm time and nonstorm substorms, and found that generally the O^+ density and pressure in the plasma sheet are a factor of 5 larger during storm time substorms than during nonstorm substorms. Using Geotail observations, *Nosé et al. (2000a)* showed that

the ionospheric O^+ in the plasma sheet are commonly more energized than H^+ ions during the substorm expansion phase. *Kistler et al. (2010)*, using the ion composition data from Cluster/CIS instrument, showed that the O^+ population displays different behaviors in different storm phases and that the enhanced O^+ ions in the plasma sheet and lobes may contribute significantly to the ring current during a storm. *Fok et al. (2006)* found rapid increases of O^+ energy density in the ring current in storms and substorms using energetic neutral atom images from IMAGE/HENA. *Nosé et al. (2005)* studied the dynamics of O^+ ions during a strong magnetic storm and found that compared to quiet intervals, the O^+ ions are significantly energized and account for more than 90% of the total energy in the near-Earth plasma sheet. *Kistler et al. (2005)* found that the O^+ ions in the current sheet contributes 5-10% of the cross-tail current during storm times as the ions non-adiabatically stream from dawn to dusk across the tail.

While the above correlating relations between the ionospheric outflow intensity and magnetic activity level has been relatively explored (i.e., a higher activity level corresponds to larger ionospheric outflow and energy content within the magnetosphere), the role of the heavy ion outflow in regulating the configuration and dynamics of the magnetosphere has not yet been well established. Such regulation includes the influence of the ionospheric heavy ion outflow on the storm ring current, the magnetotail stability, global reconnection rate, and even the coupling process with external driving (e.g., the solar wind). Furthermore, it is still unclear which outflow pathway plays a more important role in providing mass and energy sources to the plasma sheet and the ring current. Therefore, exploring the different roles of these two pathways in above regulation requires more investigations.

1.5 Dissertation structure

This dissertation focuses on the impact of interplanetary discontinuities on the MI system, including not only the **direct response of the MI system** to the suddenly impinged changes from the solar wind or IMF but also the **subsequent self-modulation within the MI system**. Particularly, the study of the direct response of the MI system will address two problems: (1) the quantification of the time delay required for a northward-to-southward IMF transition to influence the ionosphere after its arrival at the bow shock and (2) the exploration of physical processes and corresponding mechanisms that follows a strong, sudden increase of the solar wind density encountering the magnetosphere. The study of the subsequent self-modulation within the MI system (i.e., the ionospheric outflow) will explore the role of ionospheric heavy ion outflow in (1) (de)stabilizing the magnetotail and forming the storm-time ring current, (2) varying the subsolar and global reconnection rate, and (3) the feedback to the external coupling the solar wind-magnetosphere interaction.

The structure of this dissertation will be designed as follows: Chapter II describes the numerical tools utilized to study the solar wind-magnetosphere-ionosphere system; Chapter III presents the work on the quantification of the time delay between the IMF Bz discontinuity encountering the bow shock and the ionosphere undergoing disturbances; Chapter IV explores the generation mechanisms of the two-phase response after the sudden increase in solar wind pressure compresses the magnetosphere; Chapter V carries out both observational analysis and numerical simulations to understand the discrepancies among the real observations about the typical two-phase response and to further investigate the propagation of the disturbed signal within the MI system; Chapter VI concentrates on the ionospheric plasma outflow under disturbed conditions and its influence on various magnetospheric dynamics; Chapter VII is the summary of major results from the dissertation work; and Chapter VIII lists several studies for the future work.

CHAPTER II

Methodology:

Space Weather Modeling Framework

This chapter will describe the numerical tool used to investigate the physical processes of the solar wind-magnetosphere-ionosphere coupling. This chapter aims to describe a general summary of numerical models, particularly the near-Earth models needed in this dissertation. These near-Earth models are part of the Space Weather Modeling Framework (SWMF). For certain investigation which requires specific numerical configurations such as in Chapter III, IV, V, and VI, more details on the methodology will be provided there.

2.1 SWMF introduction

The Space Weather Modeling Framework (SWMF) developed at the Center for Space Environment Modeling (CSEM) at the University of Michigan currently integrates 13 physical models of various domains into one high-performance coupled model (*Tóth et al. (2005)*). These domains reside throughout the entire Sun-Earth system environment, including the Solar Eruption Generator (EG), Solar Corona (SC), Inner Heliosphere (IH), Outer Heliosphere (OH), Energetic Particles (EP), Global Magnetosphere (GM), Inner Magnetosphere (IM), Radiation Belt (RB), Ionosphere Elec-

trodynamics (IE), Plasmasphere (PS), Upper Atmosphere (UA), Polar Wind (PW), and Lower Atmosphere (LA). Each of these components can be represented by an individual mathematical model with its own dependent variables, equations of evolution, numerical schemes, and certain assumptions of the interaction with the rest of system. The influence from external domains can be accounted for by using the satellite and ground-based measurements, simplified assumptions, or other model outputs. However, the SWMF integrates all of these complex models into a framework via standardized interfaces, not only providing first-principle physics, but also enabling simulations of complicated phenomena that were not possibly captured by the individual models (*Tóth et al. (2005)*). The SWMF is capable of flexibly simulating the physics throughout the entire Sun-Earth environment, from the low solar corona through the heliosphere, the magnetosphere, and to the upper atmosphere of the Earth. With the help of large supercomputers, the efficient computational algorithms in the framework enable simulations of the Sun-Earth environment faster than real time. Figure 2.1 illustrates the 13 physical domains currently incorporated in the SWMF. The figure also demonstrates the external inputs that drive the entire framework or part of the framework, such as flare/CME observations, synoptic magnetograms, upstream monitors from ACE/WIND spacecraft measurements, F10.7 flux and gravity waves, and in-situ radar/magnetometer observations. Details about each of these components, the interlaced couplings, and the architecture of the SWMF have been provided in *Tóth et al. (2005)*. In the following section, only three components of the SWMF will be described in detail.

2.2 Near-Earth modules

The work conducted in this dissertation primarily utilizes three of the 13 modules in the SWMF: the Block-Adaptive-Tree Solar-wind Roe-type Upwind Scheme (BATS-R-US) code that simulates the global magnetosphere (GM) (*Powell et al.*

Space Weather Modeling Framework

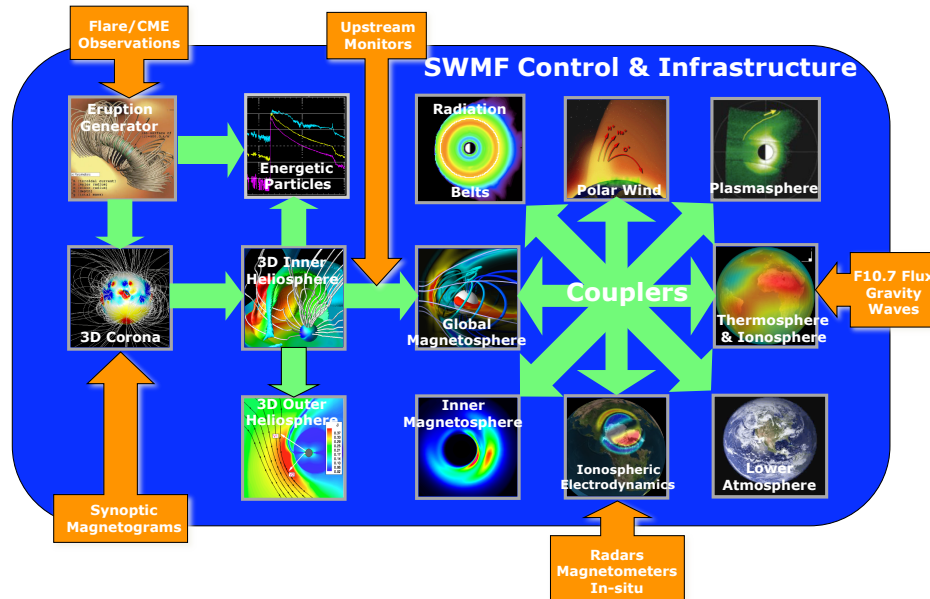


Figure 2.1: The components of the Space Weather Modeling Framework (SWMF) built in the Center for the Space Environment Modeling (CSEM).

(1999)), the model by *Ridley et al.* (2004) that describes the ionospheric electrodynamics (IE), and the Rice Convection Model (RCM) that computes the kinetic behavior of charged particles in the inner magnetosphere (IM). These three modules are coupled with each other through interfaces illustrated in Figure 2.2, providing high-performance computational ability of exploring the physical dynamics in the terrestrial system. Validation of these modules has been carried out by comparisons against a wide variety of observations, such as ground-based magnetic perturbations (*Yu and Ridley* (2008); *Yu et al.* (2010)), the Dst index and geosynchronous magnetic field measurements (*Ilie et al.* (2010)), magnetic and plasma observations from DMSP and CHAMP (*Wang et al.* (2008)), and magnetospheric magnetic fields and plasma observed by geosynchronous satellites (*Welling and Ridley* (2010)).

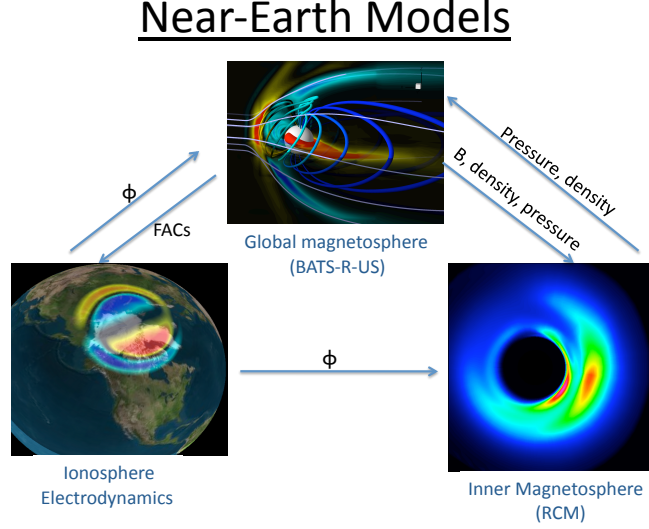


Figure 2.2: Exchange of information among GM/BATS-R-US, IM/RCM, and IE models.

2.2.1 Global magnetosphere (GM)

The global magnetosphere (GM) module not only simulates a variety of plasma boundary layers, current systems, and magnetospheric dynamics inside the magnetosphere, but also models the mass, momentum and energy coupling between the magnetosphere and the solar wind.

The GM component is numerically represented by the BATS-R-US (Block-Adaptive-Tree Solar-wind Roe-type Upwind Scheme) code, which solves the governing equations of magnetohydrodynamics (MHD). The equations for an ideal, inviscid, compressible, and perfectly conducting fluid moving at a non-relativistic speed in three dimensions consist of the macroscopic transport equations for the whole gas as a single conducting fluid together with Maxwell equations, based on the following simplified assumptions (*Gombosi (1998)*):

- The gas components are not far from local thermodynamic equilibrium. Therefore, the scalar pressure can be used, instead of a pressure tensor.

- Heat flow is neglected in the fluid.
- Charge quasi-neutrality is assumed.
- The high-frequency component of the electric field is neglected. That is, MHD describes low-frequency phenomena.
- The plasma is perfectly conducting except for numerical diffusion.

In these approximations, the equations that solve ideal MHD are:

$$\begin{aligned}
\frac{\partial \rho}{\partial t} + \mathbf{u} \cdot \nabla \rho + \rho \nabla \cdot \mathbf{u} &= 0 \\
\rho \frac{\partial \mathbf{u}}{\partial t} + \rho \mathbf{u} \cdot \nabla \mathbf{u} + \nabla \cdot \left(p \mathbf{I} + \frac{B^2}{2\mu_0} \mathbf{I} - \frac{\mathbf{B}\mathbf{B}}{\mu_0} \right) &= 0 \\
\frac{\partial \mathbf{B}}{\partial t} + \nabla \cdot (\mathbf{u}\mathbf{B} - \mathbf{B}\mathbf{u}) &= 0 \\
\frac{\partial p}{\partial t} + \mathbf{u} \cdot \nabla p + \gamma p \nabla \cdot \mathbf{u} &= 0
\end{aligned} \tag{2.1}$$

where ρ is density, \mathbf{u} is velocity, p is pressure, and B is magnetic field.

The above primitive equations are good in numerically solving smooth plasma conditions, but fail to obtain correct solutions where jump conditions (discontinuity) are present, such as at the bow shock. To avoid such situations, the conservative form of the MHD equations (Equation (2.2)) are alternatively used in the code:

$$\begin{aligned}
\frac{\partial \rho}{\partial t} + \nabla \cdot (\rho \mathbf{u}) &= 0 \\
\frac{\partial \rho \mathbf{u}}{\partial t} + \nabla \cdot \left(\rho \mathbf{u} \mathbf{u} + p \mathbf{I} + \frac{B^2}{2\mu_0} \mathbf{I} - \frac{\mathbf{B}\mathbf{B}}{\mu_0} \right) &= 0 \\
\frac{\partial \mathbf{B}}{\partial t} + \nabla \cdot (\mathbf{u}\mathbf{B} - \mathbf{B}\mathbf{u}) &= 0 \\
\frac{\partial e}{\partial t} + \nabla \cdot \left[\left(e + p + \frac{\mathbf{B} \cdot \mathbf{B}}{2\mu_0} \right) \mathbf{u} - \frac{\mathbf{B}(\mathbf{B} \cdot \mathbf{u})}{\mu_0} \right] &= 0
\end{aligned} \tag{2.2}$$

Here the conserved quantities are density ρ , momentum density $\rho \mathbf{u}$, magnetic field \mathbf{B} , and total energy density e which is the sum of thermal, kinetic, and magnetic energy

densities. Terms that deviate from ideal MHD can also be included as source terms into the right hand side (RHS) of the equations (2.1, 2.2). The source terms model diffusion, chemical reactions and other effects. For example, in the density equation, the source terms of the plasma density can be the product of ionization or the losses from charge-exchange or collisional recombination, etc. Various implementations of the MHD equations can be achieved in the BATS-R-US code by supplementing extra physics, such as semi-relativistic, resistive, Hall, multi-species, and multi-fluid MHD. Therefore the BATS-R-US model can be configured to study many different forms of magnetospheric physics.

Equations 2.2 can also be collected and written in a divergence form:

$$\frac{\partial \mathbf{U}}{\partial t} + (\nabla \cdot \mathbf{F})^T = \mathbf{S}, \quad (2.3)$$

where \mathbf{U} is the vector of conserved quantities (i.e., mass density, momentum, magnetic field, and energy), \mathbf{F} is a flux tensor:

$$\mathbf{F} = \begin{pmatrix} \rho \mathbf{u} \\ \rho \mathbf{u} \mathbf{u} + (p + \frac{\mathbf{B} \cdot \mathbf{B}}{2\mu_0}) \mathbf{I} - \mathbf{B} \mathbf{B} \\ \mathbf{u} \mathbf{B} - \mathbf{B} \mathbf{u} \\ \mathbf{u} (E + p + \frac{\mathbf{B} \cdot \mathbf{B}}{2\mu_0}) - (\mathbf{u} \mathbf{B}) \cdot \mathbf{B} \end{pmatrix},$$

and \mathbf{S} is the source term describing any diffusion, chemical reactions, radiation transport or other effects if such processes are needed in the study.

Equation (2.3) is solved in BATS-R-US code by utilizing an approximate Riemann solver with Roe-type flux and finite-volume high-resolution upwind scheme (*Powell et al. (1999)*). With finite-volume discretization, the domain is divided into a number of “cell volumes”, within which the integration of conservative variables is conserved. That is, the rate of change of a conserved physical quantity is simply the sum of

all fluxes through the faces defining the “cell volume”, plus the volume integral of the source terms, if there are any. This conservation-law based finite-volume approach enables the jump conditions across shock waves to be correctly obeyed with the help of the approximate Riemann solver with Roe-type flux. While the above equation leads to eight eigenvalue/eigenvector pairs: an entropy wave, two Alfvén waves, two magnetosonic fast waves, two magnetosonic slow waves, and an eighth eigenvalue/eigenvector pair associated with the jump of the normal component of the magnetic field (*DeZeeuw et al. (2000)*), Roe’s scheme computes the flux at cell interfaces based on the states on the left and right interfaces, constructs a numerical flux that treats each of these waves in an upwind manner, and captures the discontinuities correctly. For regions away from the discontinuities, a limited reconstruction approach ensures second-order accuracy, while meanwhile providing the stability of the nonoscillatory solutions. The detailed algorithms of solving the ideal MHD are provided by *Powell et al. (1999)* and *DeZeeuw et al. (2000)*.

This MHD code uses a block-based tree structure in Cartesian grids and adaptive mesh refinement (AMR) techniques to treat problems with disparate length scales (*Powell et al. (1999)*; *DeZeeuw et al. (2000)*). The basic underlying unit is a block of structure grid of arbitrary size, but typically, blocks of anywhere between $4 \times 4 \times 4$ and $12 \times 12 \times 12$ cells are used. Starting with an initial mesh consisting of blocks of equal size, the adaptation is accomplished by dividing or coarsening the appropriate solution blocks. Therefore, in a region that is deemed to be sufficiently interesting and requires finer resolutions, the block (“parent”) is refined by dividing itself into eight octants (“children”) evenly in each dimension; Each of the eight octants then becomes a new block. Conversely, a less interesting region may have a coarse resolution by coarsening the blocks. Figure 2.3 illustrates two neighboring blocks with different grid resolutions, with the top one one-level more refined than the bottom one. Such a block-based AMR technique is powerful in saving several orders of magnitude in

computing resources in solving problems with various length scales such as the magnetosphere. The block-based tree structure in the MHD code is also considered to be advantageous because the blocks of the grid can easily be farmed out to separate processors with communications only limited to the boundary between a block and its parent, significantly improving the massively parallel computation performance, such that doubling the number of processors allows one to run twice as fast with the same grid resolution or to run on twice as fine a mesh in the same amount of time.

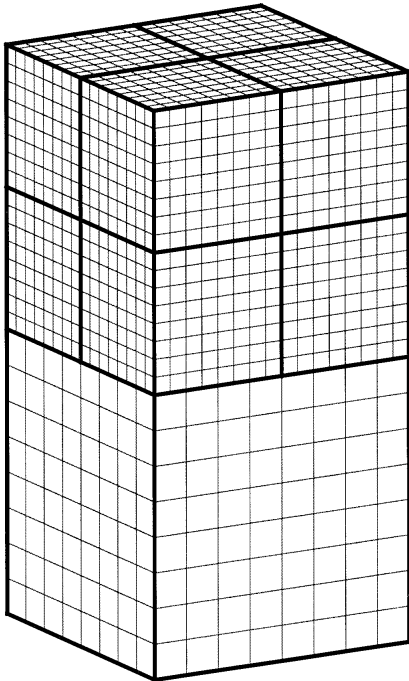


Figure 2.3: Two neighboring blocks with the top block refined into 8 blocks.

The physical domain covered by this MHD model extends from $32 R_e$ on the dayside to $224 R_e$ on the nightside in the Sun-Earth direction and $\pm 128 R_e$ in other two directions, with the inner boundary on a sphere of $2.5R_e$ away from the center of the planet. The state of the magnetosphere is controlled by the conditions in the solar wind input from the outer boundary and in the ionosphere input from the inner boundary. The streaming solar wind is imposed at the upstream outer boundary at $32R_e$. The solar wind conditions are obtained either from other model outputs or from real observations such as ACE or Wind spacecraft measurements or even from

manually designed conditions. At the other outer boundaries, zero gradient is applied to the plasma parameters because these boundaries are far enough from the planet to influence the near-planet dynamics. The inner boundary conditions of the MHD model are partially controlled by the ionospheric electrodynamics (IE) model which provides electric potential ϕ to compute the plasma convection velocity at the inner boundary through $-\nabla\phi \times \mathbf{B}/|\mathbf{B}|^2$ drift. The inner boundary also prescribes the mass density and pressure conditions needed in the MHD equations. No parallel electric potential drop is allowed in the region between the ionosphere boundary and the inner boundary of the MHD model.

Furthermore, the MHD model receives pressure/density corrections for the closed field lines region from the inner magnetosphere (IM) model, allowing the code to better represent the solutions in the near-Earth region, where the kinetic behavior of charged particles are dominant but can not be solved by a MHD code that deals with larger-scale and slowly-varying problems. In turn, BATS-R-US provides the IM module with magnetic field volume, averaged plasma density and pressure along the magnetic field lines and the IE module with field-aligned currents to drive the electrodynamics in the ionosphere.

2.2.2 Ionospheric electrodynamics (IE)

Ridley et al. (2004) incorporated a height-integrated electric potential solver into the SWMF to represent ionospheric electrodynamics. The solver utilizes the field-aligned currents (FACs) received from the global MHD model to determine the particle precipitation and conductances in the ionosphere. The conductance and FACs are then used to calculate the electric potential, which in turn prescribes plasma convections at the inner boundary of the MHD code.

The electrodynamic coupling between the GM and IE components was first proposed by *Goodman* (1995), later implemented by *Amm* (1996), and summarized

in *Ridley et al.* (2004). Here, for the sake of better understanding and comprehensive descriptions of the coupling system, the coupling procedures are listed below:

1. FACs are computed near the inner boundary of the global MHD model using $J_{\parallel} = \nabla \times \mathbf{B} \cdot \mathbf{b}$, where J_{\parallel} is FAC, \mathbf{B} is local magnetic field, and \mathbf{b} is the normal vector of the local magnetic field. The FACs are then mapped down to the ionosphere along magnetic field lines according to the relation $J_{\parallel}/B_m = J_{\parallel i}/B_i$, where $J_{\parallel i}$ is field-aligned current at the ionospheric altitude, B_m and B_i are the strengths of magnetic field at the GM inner boundary and ionosphere altitude, respectively.
2. A height-integrated ionospheric conductance tensor Σ is generated based on the FACs. The conductance tensor includes effects from several sources: solar EUV ionization, auroral energetic particle precipitation, polar rain precipitation, and nightside star light ionization. The details of obtaining the conductance tensor are described in *Ridley et al.* (2004).
3. Electric potential is then determined by the following relationship: $J_{\parallel i} \sin(I) = \nabla_{\perp} \cdot (\Sigma \cdot \nabla \phi)_{\perp}$, where I is the dip angle of the magnetic field line, Σ is height-integrated ionospheric conductance tensor, and ϕ is electric potential. This relation is derived from zero divergence of the current. The electric potential is determined in each hemisphere independently, with a boundary condition of zero potential at 5° latitude lower than the lowest latitude of the field aligned current. This boundary condition is used primarily to act in place of a shielding Region-2 current.
4. Finally the electric potential is mapped out to the inner boundary of the global MHD model along magnetic field lines. The potential is utilized to compute electric fields and then plasma velocity needed at the MHD code inner boundary.

2.2.3 Inner magnetosphere (IM)

The inner magnetosphere domain is a complex, coupled, self-modifying system, consisting of the ring current, radiation belt, and plasmasphere overlapping with each other. The domain covers the closed field-line region near the planet, mainly from the dayside magnetopause to the middle plasma sheet ($25R_e$) on the nightside. While the radiation belts contain energetic particles of MeV energy, the ring current consists of charged particles in an energy range of 10-200 KeV, carrying a large fraction of total particle energy of the magnetosphere and enough current to substantially influence the overall magnetic configuration. The ring current plays an important role in influencing the plasmasphere, radiation belt, global magnetosphere, as well as ground-based magnetic fields. The coexisting plasmasphere, however, is composed of particles with low energies. While the plasmasphere does not directly affect magnetic configuration, it contains most of the mass of the magnetosphere and can affect the wave-particle interactions, and particle sources and losses of the ring current and radiation belts. Due to a wide energy range in these different particle populations in the inner magnetosphere and differential drift of the charged particles in the ring current, the particles cannot be treated as a single fluid as done in the MHD code. The ring current is usually numerically represented by models that solve equations describing the kinetic motion of keV-energy ions and electrons:

$$\frac{\partial f}{\partial t} + \mathbf{v} \cdot \frac{\partial f}{\partial \mathbf{r}} + \mathbf{a} \cdot \frac{\partial f}{\partial \mathbf{v}} = \left(\frac{\delta f}{\delta t}\right)_{loss} + \left(\frac{\delta f}{\delta t}\right)_{diffusion}. \quad (2.4)$$

where f is distribution function. Different kinetic models interpret the distribution function f in different ways: in the Comprehensive Rice Convection Model (CRCM), $f = f(\mu, J)$ is phase space density of a particle species (Fok *et al.* (2001)), where μ is magnetic moment and J is second adiabatic invariant; in the Ring Current-Atmosphere Interaction Model (RAM), f is phase space density $Q(E, \alpha_0)$, where E is

the kinetic energy of particles, α is the equatorial pitch angle (*Jordanova et al. (1996, 1997)*); in the Rice Convection Model (RCM), $f = \eta$ is the number of particles per magnetic flux (*Wolf (1983); Toffoletto et al. (2003)*).

In the SWMF, the inner magnetosphere component can be represented by the RCM that solves time-dependent coupled equations of plasma motion for the inner magnetosphere-ionosphere system in a two-dimension closed field-line domain. The model describes the adiabatically drifting isotropic particle distribution by a number of “fluids” in a self-consistently computed electric field, given magnetic field conditions. Each fluid is characterized by an energy invariant λ_s and flux tube content η_s :

$$\begin{aligned}\lambda_s &= W_s V^{2/3} \\ \eta_s &= n_s V\end{aligned}\tag{2.5}$$

Here, W_s is kinetic energy, n_s is number density and $V = \int ds/B$ is the flux tube volume.

The simplified logical procedures in the RCM are listed below, while detailed algorithms and numerics are provided by *Sazykin (2000)* and *Toffoletto et al. (2003)*:

1. Given the initial and boundary conditions of particle density, magnetic field, and flux tube volume, the RCM code advects each fluid through the following equation:

$$\frac{\partial \eta_s}{\partial t} + \frac{\mathbf{B} \times \nabla (\Phi + \Phi_c + \frac{\lambda_s}{q_s} V^{-2/3})}{B^2} \cdot \nabla \eta_s = -L\tag{2.6}$$

Here, Φ is electric potential in the ionosphere, Φ_c is corotation potential, q_s is particle charge, and L represents explicit losses such as the charge exchange.

2. The updated flux tube content η_s is further used to compute the pressure dis-

tribution P needed in the calculation of the Birkland currents $J_{||i}$:

$$\begin{aligned} P &= \frac{2}{3}V^{-5/3}\Sigma_s\lambda_s\eta_s \\ J_{||i} &= \frac{1}{2}\mathbf{b} \cdot \nabla V \times \nabla P \end{aligned} \tag{2.7}$$

Here, \mathbf{b} is a unit vector along the magnetic field and Σ_s is the sum symbol over all the “fluids”.

3. The electric potential distribution in the ionosphere is determined from the current conservation relation ($\nabla \cdot \mathbf{J} = 0$) which is further integrated over the flux tube:

$$\nabla \cdot [-\Sigma \cdot \nabla \Phi + \mathbf{J}_w] = J_{||i} \sin(I) \tag{2.8}$$

Here, Σ is the field-line integrated conductance tensor, I is the dip angle of the magnetic field, and J_w term represents ionospheric currents caused by neutral winds and involves field line integrals of products of wind velocity and conductances. The electric potential is solved in the ionosphere from the equator to the open-closed boundary.

4. The potential is subsequently applied to Equation (2.6) to advance the flux tube content for the next time step, thereby closing the logical loop.

The RCM self-consistently computes the electric field, currents, and particle distribution in the simulation domain, given certain initial and boundary conditions. The RCM is driven by inputs such as magnetic flux tube volume distribution V and initial and boundary conditions for the plasma flux tube content η , as required for the η computation in Equations (2.6). In this framework, the IM module receives the field line flux tube volume, field-aligned averaged plasma mass density, and temperature along the field lines from the GM component throughout a simulation, first as initial conditions for the entire RCM modeling domain and later as boundary conditions only along the outer boundary of the RCM modeling domain. The IM component

also receives the electric potential from the IE module. In principle, it is not necessary for the RCM to solve the electric potential from Equation (2.8) in the coupled models, since the RCM can utilize the potential calculated in the IE module. However, due to the higher-resolution grid in the RCM, both options are implemented. The RCM in turn provides the GM component with plasma pressure to correct the pressure obtained in the global MHD code. The details about the coupling processes between the GM and IM components are described by *DeZeeuw et al. (2004)*. The coupling between RCM and BATS-R-US aims to allow the MHD model to better represent the gradient/curvature drift physics in the inner magnetosphere and therefore to better solve the Region-2 FACs that connect the ionosphere and the inner magnetosphere.

2.3 My contribution to the SWMF

The Space Weather Modeling Framework is a highly integrated framework, including a wide array of modules that represent physics throughout the Sun-Earth environment. The SWMF was developed by a large team over many years. Although the core of the SWMF and the modules were developed by others, my contribution to the SWMF is as follows:

- Validated the SWMF using ground-based magnetometer observations for nine geomagnetic storms of various activity levels. The validation is carried out by comparing the real magnetic field perturbations observed from a wide variety of ground stations against the model prediction that calculates the magnetic perturbation from ionospheric Hall currents (*Yu and Ridley (2008)*).
- Implemented a more precise solver in calculating the ground magnetic field perturbation in the MHD model BATS-R-US, by including all magnetospheric current systems, all ionospheric currents, and FACs in the “gap” region between the ionosphere model and the inner boundary ($2.5 R_E$) of the MHD model.

Validations of this new tool reveal that the prediction of mid- and low-latitude electrodynamics is significantly improved (*Yu et al. (2010)*).

- Implemented a multi-fluid coupler between the global MHD model BATS-R-US and the inner magnetosphere model RCM. Originally, only single fluid properties were exchanged between the two models, even if the global MHD model was configured to solve multi-fluid MHD. The multiple fluids are integrated into one single fluid before being passed to the inner magnetosphere model and the same for the other passing direction. Such a simplification may erase the dynamical coupling for the minor ions such as O^+ which can occasionally gain significant enhancement and put large feedback onto the magnetospheric dynamics. A multi-fluid coupler means information of the exact same individual fluid between the two models is exchanged. Therefore, the dynamics of each fluids are well prereserved during the coupling process and the subsequent evolution in either model.
- Implemented an empirical ionospheric outflow boundary for the global MHD model BATS-R-US based on a scaling formula and other observations. The scaling formula, obtained by *Strangeway et al. (2005)* using a number of FAST observations over the dayside cusp region, relates the heavy ion O^+ flux with precipitating Poynting flux or electron number density. Such an empirical outflow boundary provides another option for the modelers to study the ionospheric outflow, in addition to a constant outflow rate or self-consistently integrated global outflow as developed by *Glocer et al. (2009a)*.